Journal of Materials Chemistry C

ROYAL SOCIETY OF CHEMISTRY

PAPER

View Article Online
View Journal | View Issue

Cite this: J. Mater. Chem. C, 2022, 10, 2724

Tuning the antiaromatic character and charge transport of pentalene-based antiaromatic compounds by substitution†

Jianglin Wu,[ab] Yao Chen,[b] Jueshan Liu,[a] Zhenguo Pang,[a] Guoping Li,[b] Zhiyun Lu,[a] Yan Huang,*[a] Antonio Facchetti*[bc] and Tobin J. Marks*[b]

Received 6th July 2021,
Accepted 25th September 2021

DOI: 10.1039/d1tc03156b

rsc.li/materials-c

Understanding the structure–property relationships in antiaromatic molecules is crucial for controlling their electronic properties and designing new organic optoelectronic materials. Here we report the design, synthesis, and characterization of three new antiaromatic molecules (**Pn**, n = 1–4) based on the pentalene (P) antiaromatic core, to investigate how electron-donating and electron-accepting substituents affect **P1–P4** properties. As expected, the optical, HOMO and LUMO energy levels and electronic structure are greatly modulated by core substitution. Compared to the unsubstituted compound (**P1**), **P3** and **P4** containing strong electron-withdrawing units reduced antiaromaticity as assessed by nucleus-independent chemical shift (NICS) calculations compared with **P2**, which is functionalized with strong electron-donating units, showing that substitution strongly tunes local antiaromaticity. Organic field-effect transistors (OFETs) fabricated using these materials indicate that **P2** has an average hole mobility of $\sim 10^{-4}$ cm^2 V^{-1} s^{-1} while **P3** has an average electron mobility of up to 0.03 cm^2 V^{-1} s^{-1}, *versus* FET-inactive **P1**. Therefore, introduction of strong π-extended electron-withdrawing or electron-donating substituents onto an antiaromatic core is an effective strategy to switch-on charge transport capacity.

1 Introduction

Aromaticity is a fundamentally important and intriguing property of numerous organic chemical structures and has stimulated a myriad of experimental and theoretical investigations.[1–3] Since Hückel first codified the $(4n + 2)$ π-electron rule for monocyclic rings as the guideline for aromaticity,[4] additional aromatic mono/oligocyclic rings have been reported[5–7] and investigated in research fields as diverse as materials science,[8–10] photonics,[11–13] agriculture, pharmaceuticals,[14] and biomedicine.[15] Antiaromaticity, where $(4n)$ π-electrons are present in a conjugated cyclic structure, as the inverse concept of aromaticity, was first proposed by Breslow in 1967.[16] Unlike aromaticity, antiaromaticity leads to structural destabilization, paratropic ring currents, and π-bond localization.[17–19] Importantly, it has been suggested that antiaromaticity can compress the highest occupied molecular orbital (HOMO)–lowest unoccupied molecular orbital (LUMO) energy gap and potentially promote carrier mobility in organic semiconductors, which is desirable for application in a number of organic electronic device classes,[20–22] such as organic solar cells (OSCs)[23,24] and organic field-effect transistors (OFETs).[20,25–28] Through important design contributions both from synthetic and theoretical chemists, diverse antiaromatic molecule classes have been developed, including pentalenes,[29,30] indacenes,[31,32] cyclooctatetraenes,[33,34] and their derivatives.[35–37] However, compared to the literature of aromatic compounds, optoelectronic investigations of antiaromatic materials remain far more limited, primarily due to the modest stability of typical antiaromatic compounds[38] and challenges in their chemically modification, which has typically involved fusion with aromatic rings,[19,39] replacement of C–C bonds with isosteric B–N bonds,[40] and aromatic ring functionalization.[41,42]

Tuning the antiaromatic character and substitution pattern in antiaromatic molecules *via* structural modification is essential for achieving specific functions. For example, Xia *et al.* tuned the aromatic character of fused cyclobutadienoids by changing the fusion pattern[43] while Yasuda *et al.* enhanced the antiaromatic character of pentalene by benzoannulation.[44] Yamaguchi *et al.* reported that the antiaromaticity and

[a] Key Laboratory of Green Chemistry and Technology (Ministry of Education), College of Chemistry, Sichuan University, Chengdu 610064, P. R. China. E-mail: huangyan@scu.edu.cn
[b] Department of Chemistry, Center for Light Energy Activated Redox Processes (LEAP), Materials Research Center (MRC), Northwestern University, 2145 Sheridan Road, Evanston, Illinois 60208, USA. E-mail: t-marks@northwestern.edu, a-facchetti@northwestern.edu
[c] Flexterra Inc., 8025 Lamon Avenue, Skokie, IL 60077, USA

† Electronic supplementary information (ESI) available: Synthesis, computation, and characterization details. CCDC 2042122 and 2042120. For ESI and crystallographic data in CIF or other electronic format see DOI: 10.1039/d1tc03156b

electronic properties of the pentalene core could be widely tuned by the degree of aromatic character of the peripherally fused rings.[29] Nevertheless, the above-mentioned molecular strategies required considerable demanding synthetic efforts.

The realization of organic molecules having optimally placed selected donor (D)–acceptor (A) moieties/functionalities is a proven design strategy to achieve organic semiconductors for opto-electronics since the electronic structure, optical absorption, energy levels, and solid-state packing can be tuned to the greatest extent. Indeed, numerous high-performance organic semiconductors for OSCs,[45–47] OFETs,[48–50] organic light-emitting diodes (OLEDs),[51] and organic sensors[52,53] have such D–A cores and/or substituent patterns.

In marked contrast, D–A antiaromatic compounds are extremely rare.[54–58] Furthermore, to the best of our knowledge, there have been no systematic investigations of semiconducting D–A antiaromatic structures. Pentalene, consisting of two fused cyclopentadiene rings with 8π electrons, is one of the most important antiaromatic rings.[59] Although pentalene itself is thermally unstable and rapidly dimerizes above −196 °C,[60] a growing list of aryl-fused pentalenes are known to be quite stable owing to the delocalization of the pentalene double bonds into the adjacent aromatic subunits, such as dibenzo[*a*,*e*]pentalene (DBP),[61,62] dithieno[*a*,*e*]pentalene (DTP),[63] naphthopentalene (NPP).[64] In this study, we synthesized the new molecular structures **P2–P4** using the DTP skeleton as the antiaromatic core, benzene rings as π-bridge units, and *N*,*N*-dimethylamine, dicycanovinylindan-1-one (IC), and 5,6-difluroinedicycanovinylindan-1-one (IC2F) as the terminal donor and acceptor substituents, respectively (Fig. 1a). Our results indicate that introducing electron-donating units into the DTP core enhances the antiaromaticity of the pentalene ring, while functionalization with electron-withdrawing units reduces pentalene antiaromaticity as accessed by NICS calculations. The new compounds were characterized by single-crystal X-ray diffraction analysis, ultraviolet-visible (UV-Vis) spectrophotometry, and cyclic voltammetry (CV) measurements. Furthermore, the D/A substituents significantly modulate the HOMO and LUMO energy levels from (−5.16)–(−3.39) eV to (−4.64)–(−3.73) eV, respectively, as well as tune optical absorption maxima by more than 120 nm. Finally, the charge transport properties of **P3** were measured in TFT devices, demonstrating that these compounds can function as n-type semiconductors (*vide infra*).

2 Results and discussion

2.1 Molecular design and synthesis

The parent **P1** unit and new antiaromatic molecules **P2–P4** (Fig. 1a) were synthesized according to the routes shown in Fig. 1b using the stable and easily accessible DTP unit as the central antiaromatic core, the phenyl ring as a π-bridge, and strong electron-donating *N*,*N*-dimethylamine and strong electron-withdrawing IC and IC2F as terminal groups in the

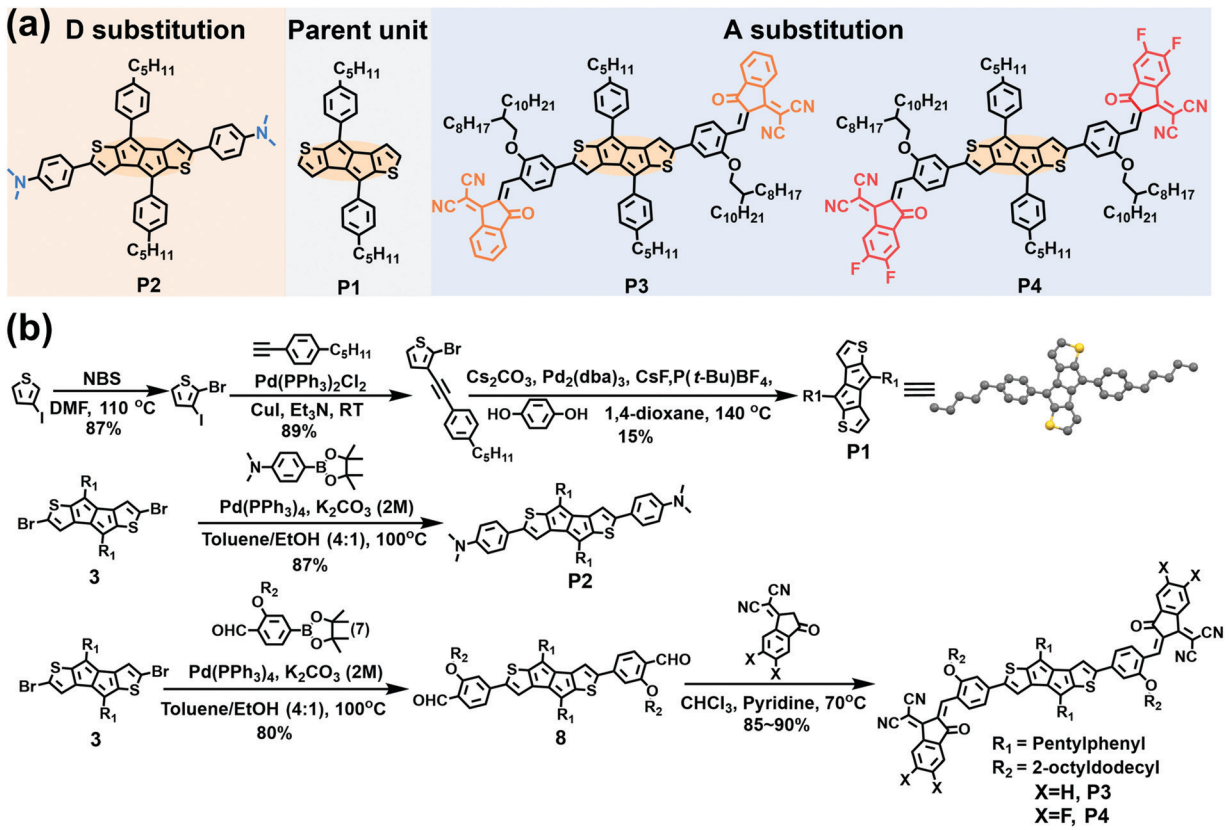

Fig. 1 (a) The molecular structures and (b) the synthetic routes to the compounds discussed in this study.

para-phenyl position. To ensure processability in common organic solvents, long alkoxy side chains (2-octyldodecyl) were introduced at the phenyl *meta*-position of the π-extended molecules **P3** and **P4**. **P1** was synthesized according to the literature by replacing the hexylphenyl with a pentylphenyl moiety.[63] The key intermediates **3** and **7** were synthesized according to literature methodologies.[63,65] Suzuki coupling reactions of compounds 7 and 4-aminophenyl boronic acid pinacol ester with compound **3** afforded compounds **8** and **P2** in 85% and 80% yields, respectively. Finally, compounds **P3** and **P4** were obtained as black solids through Knoevenagel condensation of compound **8** with IC and IC2F (85% and 90% yields), respectively. The molecular structures of compounds **P1–P4** were accessed by ^{1}H and ^{13}C NMR spectroscopy and high-resolution mass spectrometry (see Section S7 in the ESI†). The thermal properties of pentalene compounds were characterized by Thermogravimetric Analysis (TGA) and Differential Scanning Calorimetry (DSC) (Fig. S7 and S8, Table S2, ESI†). TGA demonstrates that the thermolysis onset temperatures of **P1**, **P2**, **P3** and **P4** are 300, 300, 320, and 306 °C, respectively (Fig. S7 and Table S2, ESI†). In addition, DSC analysis indicates clear melting points for **P1**, **P2**, and **P4** (171, 261 and 189 °C), respectively, but not for **P3** (Fig. S8 and Table S2, ESI†). The TGA and DSC data indicate that **P1–P4** possess good thermal stability, necessary for OFET and OSC fabrication.

2.2 Single-crystal structural analysis

We attempted to grow single crystals of all compounds using various solvent systems and succeeded in obtaining single crystals suitable for X-ray diffraction analysis for **P1** and **P2**. The crystal structures of **P1** and **P2**, shown in Fig. 2 and Fig. S2 (ESI†), indicate that both compounds are substantially planar with the pentylphenyl group having moderate dihedral angles (∼30° for **P1** and **P2**) with respect to the DTP core. Both **P1** and **P2** pentalene cores exhibit the presence of double and single-bond alternation, a common characteristic of antiaromatic molecules,[41,62] demonstrating that the intrinsic pentalene antiaromaticity is not diminished upon introducing strong electron-donating D substituents. However, the degree of bond length alternation in the pentalene unit of **P2** (1.383(3) *vs.* 1.479(3) Å) is slightly reduced compared to that in **P1** (1.373(3) *vs.* 1.484(3) Å), suggesting that the π-electron delocalization in the pentalene cores of **P2** is greater than that in **P1**, which may be due to the greater π-system extension in **P2**. Interestingly, the pentalene cores in **P1** molecules do not stack closely and exhibit only weak secondary π-edge interactions, with the minimum core–core π–π intermolecular distance being ∼3.73 Å. In contrast, the **P2** molecules stack in a brick-wall fashion (Fig. 2b, c, and Fig. S3, ESI†) with a minimum π–π core–core distance of only ∼3.37 Å, demonstrating stronger intermolecular interactions, likely due to the more expansive conjugated core.

2.3 Optoelectronic properties

The optical properties of the present compounds were investigated by ultraviolet-visible (UV-Vis) absorption spectra in both

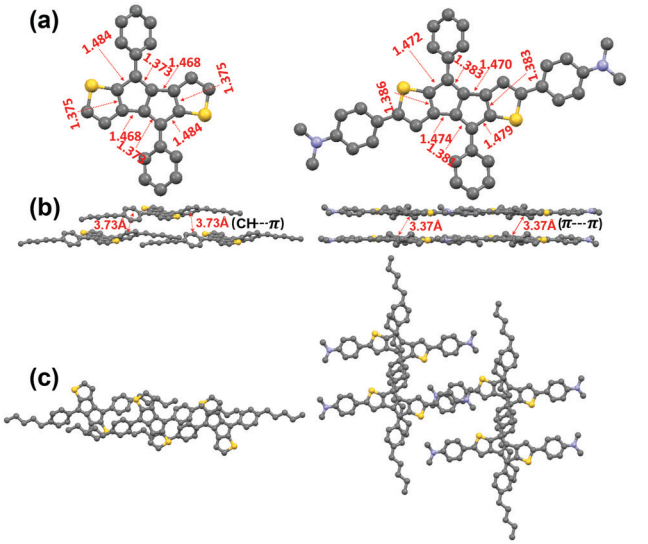

Fig. 2 X-Ray crystal structures of **P1** (left) and **P2** (right). (a) Top view and (b) Packing diagram showing **P1** π-edge and **P2** π–π interactions (b and c). In Fig. 2a the *n*-pentyl chains are omitted for ease of viewing.

dilute $CHCl_3$ solutions (5×10^{-6} M) and as thin-films spin-coated from chloroform solutions. The solution UV-Vis spectra in Fig. 3a indicate that all compounds have three distinct absorption bands, one at low energies, ∼500 nm for **P1**; 583–646 nm for **P2–P4**, one at intermediate energies in the 380–470 nm range, and a set at higher energies ranging from 330 to 360 nm. To assign these transitions, we carried out electronic structure computations at the B3LYP/6-311G(d) level. To reduce the computational demands, the long side chains of all molecules were replaced by methyl or methoxy groups. As shown in Fig. S9 (ESI†), the low energy absorption bands of **P1–P4** are assigned to HOMO−1 → LUMO transitions. In contrast to **P1** in which the low energy absorption is assigned to a locally excited (LE) transition, in **P2–P4** they are assigned to charge transfer (CT) transitions (Fig. S10, ESI†). The second absorption bands from 380 to 470 nm can be assigned to the HOMO−2 → LUMO transition, while the highest energy absorption bands from 330 to 360 nm can be primarily attributed to the HOMO → LUMO+1, HOMO−4 → LUMO+1, HOMO−14 → LUMO, and HOMO−16 → LUMO transitions for **P1** to **P4**, respectively. Note that according to Fig. S9 (ESI†),

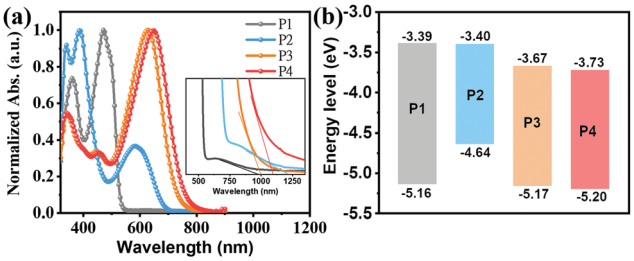

Fig. 3 (a) Solution optical absorption spectra (inset shows a magnified view at long wavelengths) and (b) energy level diagram of the indicated compounds.

the $S_0 \rightarrow S_1$ transition bands of **P1–P4**, assignable to the HOMO → LUMO transition are symmetry–forbidden, which is typical of antiaromatic molecules.[64,66] Compared with the **P1** $S_0 \rightarrow S_2$ transition, **P2–P4** exhibit red-shifted low-energy absorption ranging from 113 nm to 176 nm, which is assigned to intramolecular charge transfer (ICT) between the central core and the D/A substituents, a common feature of D–A structured molecules.[67] In addition, as shown in Fig. 3a, the **P4** low-energy absorption is redshifted by ~20 nm *vs.* the **P3** in $S_0 \rightarrow S_2$ transition, which is attributed to the stronger ICT effect caused by the fluoro-substitution.[68] Interestingly, compared to the **P1** $S_0 \rightarrow S_2$ transition, the introduction of electron-deficient units into the DTP core in **P3** and **P4** enhances molar absorption coefficient, consistent with the DFT results (Fig. S9, ESI†). These data demonstrate that introducing D–A motifs into an antiaromatic molecular unit is effective in overcoming the low absorptivity of antiaromatic molecules.[29]

The redox properties of **P1–P4** were investigated by cyclic voltammetry (CV) measurements in CH_2Cl_2 (Fig. 3b and Fig. S6 (ESI†); Table 1). From the CV data, the frontier molecular orbital energy levels were estimated from the redox potentials. Thus, the oxidation and reduction potentials of **P1–P4** were found to be +0.36, −0.16, +0.37, and +0.40 eV, and −1.41, −1.40, −1.13, −1.03 eV, respectively. Thus, the HOMO energy levels of **P1**, **P3**, and **P4** remain in a narrow range (~−5.16 eV) while that of **P2** is substantially higher (−4.64 eV). In contrast, the LUMO energy levels of **P1** and **P2** (~−3.40 eV) and those of **P3** and **P4** (~−3.70 eV) are similar, but far deeper. These results are in agreement with the presence of the electron-donating substituents ($N(CH_3)_2$) in **P2** and the strong electron-withdrawing substituents (IC and IC2F) in **P3** and **P4**, respectively. The optical bandgap substantiates this picture as well (Table 1). These data indicate that **P2** could be a hole transporting/donor semiconductor while **P3** and **P4** could be electron transporting/acceptor semiconductors in OFET/OSC devices.

2.4 Aromaticity studies

To investigate the effect of the D–A structure on the aromatic character of the DTP central unit, we carried out nucleus-independent chemical shift (NICS-XY) surveys and computed the induced ground state (S_0) current density (ACID). Further details are shown in Section S3.1 of the ESI.† To summarize the literature, antiaromatic rings are characterized by (1) paratropic ring currents as determined by positive NICS values, and (2) anticlockwise ring currents revealed *via* ACID plots.[19] As shown in Fig. 4 and Table S4 (ESI†), the NICS value of the pentalene core (a and a′ rings) of **P1** (δ18.2 ppm) is larger than that of **P3** (δ15.3 ppm). Furthermore, **P4** with a more electron-deficient unit, exhibits a lower NICS value than **P3** (δ14.8 *vs.* δ15.3 ppm). These results suggest that the introduction of an electron-deficient group on the DTP core can reduce the pentalene unit antiaromatic character, with the antiaromatic character showing a negative relationship with the degree of A unit electron-deficiency. In contrast, **P2** containing a strong electron-donating group exhibits an enhanced antiaromatic character with a higher NICS value of δ20.4 ppm. However, compared to **P1**, the effective conjugation of both D–A **P3** and **P4** compounds is extended. Thus, to understand the effects of extended conjugation on the antiaromaticity of the pentalene core, we carried out additional computations for other pentalene compounds with a **P1** core and having –OCH_3 (**P1**–OCH_3, a weak electron-donating group) and –$NH(CH_3)_2^+$ (**P1**–$NH(CH_3)_2^+$, a strong electron-withdrawing group) substituents. The results, shown in Fig. S11 (ESI†), indicate that **P1**–OCH_3 exhibits similar NICS values to that of **P1** despite the former having a more extended effective conjugation than **P1**, indicating that extended effective conjugation minimally affects antiaromaticity in these systems. However, computations on electron-deficient compound **P1**–$NH(CH_3)_2^+$ indicate that it exhibits considerably reduced NICS values *vs.* **P1**, further confirming the present conclusions that the introduction of electron-deficient substitutes will decrease antiaromaticity. These results argue that the pentalene core antiaromaticity can be tuned *via* the electron-donation ability or degree of electron-deficiency of the D or A units in the D–A structure. To understand the ring currents in the present compounds, ACID calculations were also carried out to visualize the local

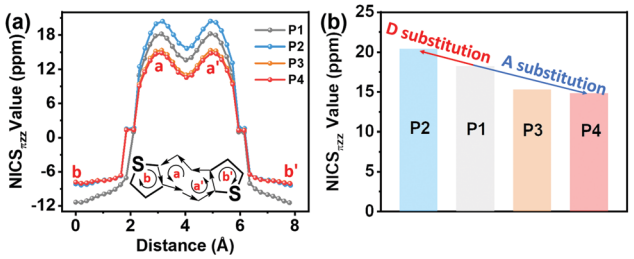

Fig. 4 The NICS-XY scans (a) and pentalene core NICS values (b) of the indicated compounds involved in this study.

Table 1 Electrochemical and optoelectronic properties of compounds **P1–P4**

Compd	$\lambda_{abs}{}^a$ (nm) (log ε)	$\lambda_{abs}{}^b$ (nm)	E_{ox} (eV)	E_{red} (eV)	HOMO^c (eV)	LUMO^d (eV)	$E_g^{cv\,e}$ (eV)	HOMO^f (eV)	LUMO^g (eV)
P1	470 (4.26)	513	0.36	−1.41	−5.16	−3.39	1.77	−5.13	−2.91
P2	583 (4.09)	622	−0.16	−1.40	−4.64	−3.40	1.24	−4.60	−2.86
P3	626 (4.89)	656	0.37	−1.13	−5.17	−3.67	1.50	−5.26	−3.37
P4	646 (4.98)	683	0.40	−1.03	−5.20	−3.73	1.47	−5.30	−3.45

[a] Measured in 5.0×10^{-6} mol L^{-1} $CHCl_3$ solution. [b] Thin films cast from $CHCl_3$ solution onto quartz substrates. [c] HOMO energy levels were estimated from the equation HOMO = $-(E_{ox} + 4.80)$ eV. [d] LUMO energy levels were estimated from the equation LUMO = $-(E_{red} + 4.80)$ eV. [e] $E_g^{cv} = E_{LUMO} - E_{HOMO}$. [f] HOMO energy levels computed by DFT. [g] LUMO energy levels computed by DFT.

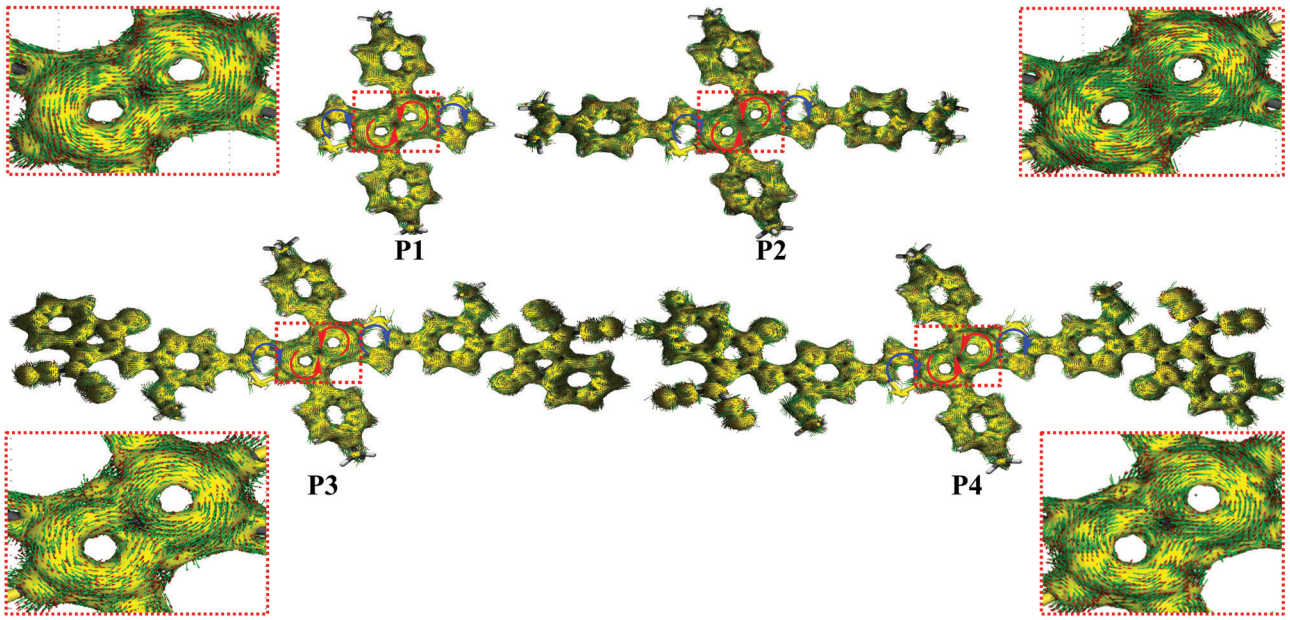

Fig. 5 Computed ring currents for the indicated molecules.

paratropic and diatropic ring currents induced by local antiaromaticity and aromaticity. As shown in Fig. 5, a counter-clockwise ring current is observed in both pentalene five-membered rings for all compounds, indicative of the strong paratropicity, and thus the antiaromaticity of this unit, which is consistent with the structural results of the single crystal diffraction analysis. In contrast, a clockwise diatropic ring current was visualized in the fused thiophene, in agreement with the NICS calculations.

2.5 OFET transport characterization

The charge transport properties of **P1**–P4 were assessed by fabricating thin-film FET devices. Unfortunately, **P4** is too insoluble to afford continuous films suitable for FET evaluation.[69,70] For **P1** and **P3** top-gate/bottom-contact (TGBC) FETs were characterized in a device configuration of, substrate (glass)/source–drain (Cr/Au/thiol)/semiconductor/dielectric (PMMA)/gate (Al). Here, 4-methoxy thiophenol was used as a self-assembled monolayer (SAM) to modify the source and drain electrode surfaces to increase charge injection.[71] However, since **P2** has good solubility in common solvents used for depositing the PMMA dielectric, such as 2-butanone and ethyl acetate, Bottom-Gate Top-Contact (BGTC) FET structures [(Si)/dielectric (SiO_2)/semiconductor/source–drain (Au)] were used for this study.

Based on survey experiments, **P1** was found to be FET-inactive while **P2** is a p-type semiconductor with an average hole mobility of $\sim 10^{-4}$ cm^2 V^{-1} s^{-1} (Fig. S12 and S13, ESI†). Compound **P3** could be effectively processed by spin-coating from $CHCl_3$ solutions (4 mg mL^{-1}) and the as-cast films exhibit n-type transport with an electron mobility (μ_e) of 0.014 cm^2 V^{-1} s^{-1}. The OFET performance of **P3** was further optimized by thermally annealing the semiconductor films at various temperatures; see details in Fig. 6a and S14 and Table S5 (ESI†). Thus, it was found that the μ_e of **P3** devices annealed over the 130–200 °C range maximizes to 0.03 cm^2 V^{-1} s^{-1} after thermal annealing at 180 °C for then falls to 0.025 cm^2 V^{-1} s^{-1} at 200 °C.

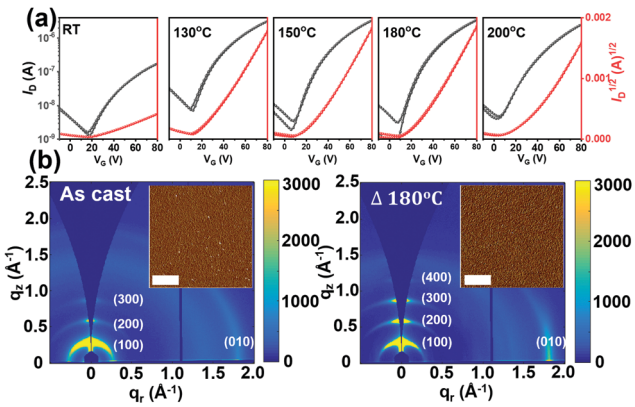

Fig. 6 (a) Transfer plots of **P3**-based OFET devices of **P3** upon thermal annealing at the indicated temperatures, RT, 130, 150, 180, and 200 °C. (b) 2D-GIWAXS and AFM (insert) images of **P3** films as casted and upon annealing at 180 °C. The scale bar of the AFM images is 1 μm.

To understand the effect of thermal annealing on the **P3** semiconductor film structure and charge transport properties, AFM and two-dimensional grazing incidence wide-angle X-ray scattering (2D-GIWAXS) measurements were carried out. The AFM height images (Fig. S16, ESI†) indicate that the pristine and all thermally annealed **P3** films exhibit smooth surfaces with small roughness values (σ_{RMS}) of 0.55–1.08 nm. Compared with the pristine **P3** films, which exhibit small aggregates, an obvious fibrillar nanostructure is observed for all the annealed films, suggesting greater crystallinity, which was further

confirmed by the 2D-GIWAXS results. For better comparison, the 2D-GIWAXS images of the pristine film and the optimized film annealed at 180 °C are shown in Fig. 6b and the corresponding one-dimensional line cuts are shown in Fig. S17 (ESI†). **P3** exhibits a pronounced (100) reflection at q_{xy} = 0.30 Å^{-1} and a (010) reflection at q_z = 1.78 Å^{-1}, corresponding to the lamellar stacking distance (dl) of 20.93 Å and π–π stacking distance ($d\pi$) of 3.53 Å. Upon thermal annealing at 180 °C, the diffraction patterns are dramatically intensified, a result in agreement with the AFM analysis and enhanced OTFT electron mobilities.

Finally, we note that the molecular design of **P3** and **P4**, and the position of their LUMO energies, suggests potential in bulk-heterojunction solar cells. Thus, we screened blends based on two donor polymers, **P3**HT and PTB7; however the OSC power conversion efficiencies were very low (Fig. S15b, c and Table S6, ESI†) and at the best approaching ∼0.02%. The poor performance reflects the low solubility of **P4** and the poor energy matching (high HOMO, low bandgap) of these molecules with common donor polymers, preventing efficient charge separation (see details in the ESI†). Furthermore, the frontier molecular orbital topologies of **P3** and **P4**, and particularly the LUMO, are mainly localized on the pentalene core, which differs considerably from that of high performance NFAs (*e.g.*, Y6) where the LUMO delocalizes on whole molecule enabling good electron transport.

3. Conclusions

A series of new antiaromatic compounds with pentalene antiaromatic cores, substituted with π-extended electron-donating and electron-accepting groups, were synthesized and characterized by a variety of methods. From optical and CV measurements, the bandgap and HOMO and LUMO energy levels can be efficiently tuned by introducing electron-donating and electron-withdrawing units, with the latter resulting in strong, red-shifted absorption and deeper energy levels. Single crystal diffraction data and DFT calculations demonstrate that introduction of strong electron-donating units enhances the antiaromatic character of the pentalene central core, while the introduction of electron-withdrawing units diminishes it. Charge transport in OFETs was also investigated, demonstrating that introduction of strong electron-donating substituent in **P2** and electron-withdrawing units in **P3** results in p-type and n-type charge transport, respectively, in accord with common trends for aromatic π-conjugated cores. Thus, these results indicate that the design and exploration of new antiaromatic molecular cores is promising for further expanding the scope of organic semiconductors in opto-electronics technologies.

4. Experimental

4,8-Di(4-pentylphenyl)-2,6-dithia-dicyclopenta[*a*,*e*]-pentalene (P1)

A mixture of **2** (3.6 g, 10.8 mmol), hydroquinone (2.38 g, 21.6 mmol), Cs_2CO_3 (7.04 g, 21.6 mmol), CsF (3.28 g, 21.6 mmol), $Pd_2(dba)_3$ (197.8 mg, 0.216 mmol), and [(*t*-Bu)$_3$PH]BF_4 (188 mg, 0.65 mmol) in anhydrous 1,4-dioxane (80 mL) was heated at 140 °C under Ar for 48 h. After cooling to room temperature, the mixture was filtered and the collected solid washed thoroughly with chloroform. The filtrate was then collected and evaporated to dryness. The residue was purified by chromatography on silica gel to give the titled product as a brown solid (0.40 g, 14.6%). ^{1}H NMR (500 MHz, $CDCl_3$, δ): 7.53 (d, J = 8.0 Hz, 4H, ArH), 7.24 (d, J = 8.0 Hz, 4H, ArH), 6.81 (d, J = 4.8 Hz, 2H, ArH), 6.70 (d, J = 4.8 Hz, 2H, ArH), 2.64 (t, J = 8.0 Hz, 4H, CH_2), 1.68–1.61 (m, 4H, CH_2), 1.59–1.31 (m, 8H, CH_2), 0.91 (t, J = 7.6 Hz, 6H, CH_3). ^{13}C NMR (125 MHz, $CDCl_3$, δ): 148.16, 144.80, 142.57, 139.04, 137.00, 130.60, 128.83, 127.64, 127.17, 121.25, 35.96, 31.55, 30.97, 22.55, 14.03. MALDI-TOF MS: calcd for $C_{34}H_{35}S_2$ (M + H$^+$): 507.2180, found (M + H$^+$): 507.2177.

4,4′-(4,8-Bis(4-pentylphenyl)pentaleno[2,1-*b*:5,4-*b*′]dithiophene-2,6-diyl)bis(*N*,*N*-dimethylaniline) (P2)

A mixture of **3** (100 mg, 0.15 mmol), *N*,*N*-dimethyl-4-(4,4,5,5-tetramethyl-1,3,2-dioxaborolan-2-yl)-aniline (111.5 mg, 0.45 mmol), $Pd(PPh_3)_4$ (6.4 mg, 0.006 mmol) and K_2CO_3 (2 M) (0.4 mL, 0.8 mmol) in a solvent mixture of toluene (10 mL) and water (2 mL) was heated at 100 °C under argon for 24 h. After cooling to room temperature, the solvent was removed *in vacuo* and the residue was purified by chromatography on silica gel to give the product as a dark green solid (89 mg, 80%). ^{1}H NMR (600 MHz, $C_2D_2Cl_4$, δ): 7.63 (d, J = 7.8 Hz, 4H, ArH), 7.41 (d, J = 7.8 Hz, 4H, ArH), 7.33 (d, J = 7.8 Hz, 4H, ArH), 6.80 (s, 2H, ArH), 6.75 (d, J = 7.8 Hz, 4H, ArH), 3.02 (s, 12H, CH_3), 2.74 (t, J = 7.8 Hz, 4H, CH_2), 1.82–1.73 (m, 4H, CH_2), 1.53–1.42 (m, 8H, CH_2), 1.00 (t, J = 7.2 Hz, CH_3). ^{13}C NMR (150 MHz, $C_2D_2Cl_4$, δ):150.4, 144.8, 131.0, 128.8, 127.9, 126.2, 123.6, 115.9, 112.8, 40.4, 36.0, 31.6, 30.6, 22.5, 13.9. MALDI-TOF MS: calcd for $C_{50}H_{52}N_2S_2$ (M$^+$): 744.3572, found (M$^+$): 744.3568.

2,2′-((2Z,2′*Z*)-(((4,8-Bis(4-pentylphenyl)pentaleno[2,1-*b*:5,4-*b*′]dithiophene-2,6-diyl)bis(2-((2-octyldodecyl)oxy)-4,1-phenylene))bis(methanylylidene))bis(3-oxo-2,3-dihydro-1*H*-indene-2,1-diylidene))-dimalononitrile (P3)

Pyridine (0.1 mL) was added to a solution of **8** (100 mg, 0.076 mmol) and IC (118 mg, 0.62 mmol) in dry $CHCl_3$ (10 mL) under argon. The mixture was heated to reflux for 8 h and then allowed to cool to room temperature. After addition of 20 mL methanol a solid formed which was collected by filtration. The crude product was purified by recrystallization with mixture of chloroform and methanol to obtain the pure compound as a dark green solid (107 mg, 85%). ^{1}H NMR (600 MHz, $C_2D_2Cl_4$, δ): 9.10 (s, 2H, CH), 8.75 (d, J = 7.8 Hz, 2H, ArH), 8.50 (d, J = 8.4 Hz, 2H, ArH), 7.97 (d, J = 7.2 Hz, 2H, ArH), 7.85 (t, J = 7.8 Hz, 2H, ArH), 7.80 (t, J = 7.2 Hz, 2H, ArH), 7.69 (d, J = 7.8 Hz, 4H, ArH), 7.42 (d, J = 7.8 Hz, 4H, ArH), 7.27 (d, J = 8.4 Hz, 2H, ArH), 7.18 (s, 2H, ArH), 7.06 (s, 2H, ArH), 4.10 (d, J = 6.0 Hz, 4H, CH_2), 2.78 (t, J = 7.8 Hz, 4H, CH_2), 2.02–1.97 (m, 2H, CH), 1.83–1.77 (m, 4H, CH_2), 1.60–1.54 (m, 4H, CH_2), 1.54–1.44 (m, 16H, CH_2), 1.41–1.26 (m, 48H, CH_2), 1.05–0.92 (m, 18H, CH_3). ^{13}C NMR (150 MHz, $C_2D_2Cl_4$, δ): 180.0, 161.0,

150.5, 150.4, 146.5, 144.0, 142.4, 141.3, 140.0, 139.5, 138.5, 137.8, 129.2, 128.2, 128.0, 124.2, 122.0, 121.8, 119.4, 119.0, 116.6, 114.0, 108.1, 73.1, 71.7, 36.1, 31.9, 31.8, 30.6, 30.0, 29.7, 29.3, 27.1, 22.6, 22.5, 14.0. MALDI-TOF MS: calcd for $C_{112}H_{130}N_4O_4S_2$ (M^+): 1658.9534, found (M^+): 1658.9534.

2,2′-((2*Z*,2′*Z*)-(((4,8-Bis(4-pentylphenyl)pentaleno[2,1-*b*:5,4-*b*′]dithiophene-2,6-diyl)bis(2-((2-octyldodecyl)oxy)-4,1-phenylene))bis(methanylylidene))bis(5,6-difluoro-3-oxo-2,3-dihydro-1*H*-indene-2,1-diylidene))dimalononitrile (P4)

P4 was prepared as a dark solid with a yield of 90% using the same procedure used for the synthesis of **P3**, but with IC2F rather than IC as the reactant. ^{1}H NMR (600 MHz, $C_2D_2Cl_4$, δ): 9.12 (s, 2H, CH), 8.62–8.56 (m, 2H, ArH), 8.50 (d, J = 8.4 Hz, 2H, ArH), 7.72 (t, J = 7.8 Hz, 2H, ArH), 7.68 (d, J = 8.4 Hz, 2H, ArH), 7.42 (d, J = 7.8 Hz, 4H, ArH), 7.26 (d, J = 8.4 Hz, 2H, ArH), 7.18 (s, 2H, ArH), 7.06 (s, 2H, ArH), 4.10 (d, J = 5.4 Hz, 4H, CH_2), 2.79 (t, J = 7.8 Hz, 4H, CH_2), 2.03–1.98 (m, 2H, CH), 1.83–1.77 (m, 4H, CH_2), 1.60–1.42 (m, 16H, CH_2), 1.40–1.29 (m, 48H, CH_2), 1.02 (t, J = 7.2 Hz, 6H, CH_3), 0.96–0.92 (m,12H, CH_3). ^{13}C NMR (150 MHz, $C_2D_2Cl_4$, δ): 184.1, 161.4, 150.9, 146.4, 146.0, 144.0, 142.5, 139.5, 138.3, 135.5, 130.1, 129.2, 128.0, 127.0, 121.6, 119.6, 116.8, 114.2, 113.5, 107.6, 73.2, 72.2, 36.1, 31.9, 31.8, 31.6, 30.6, 30.0, 29.6, 29.3, 27.1, 22.6, 22.5, 14.0, 13.9. MALDI-TOF MS: calcd for $C_{112}H_{126}F_4N_4O_4S_2$ (M^+): 1730.9157, found (M^+): 1730.9139.

Conflicts of interest

There are no conflicts to declare.

Acknowledgements

We acknowledge the financial support for this work from the National Natural Science Foundation of China (project no. 21875148) (Y. H., Z. L., J. W., J. L.). T. M., A. F., and Y. C., J. W. are grateful to the Center for Light Energy Activated Redox Processes (LEAP), an Energy Frontier Research Center funded by the US Department of Energy (DOE), Office of Science, Office of Basic Energy Sciences under award DE-SC0001059 (J. W.: fabricating device and other characterization, Y. C. and G. Li: materials synthesis, A. F. and T. J. M.: project advising), AFOSR grant FA9550-18-1-0320, the Flexterra Corporation, and the Office of Naval Research Contract N00014-20-1-2116. The use of the Advanced Photon Source, an Office of Science User Facility operated by the US DOE Office of Science by Argonne National Laboratory, was supported by the US DOE under contract DE-AC02-06CH11357. J. W. acknowledges the joint-PhD program supported by the China Scholarship Council (No. 201906240142) for a fellowship.

Notes and references

1 Z. Zeng, X. Shi, C. Chi, J. T. L. Navarrete, J. Casado and J. Wu, *Chem. Soc. Rev.*, 2015, **44**, 6578–6596.
2 J. K. Pagano, J. Xie, K. A. Erickson, S. K. Cope, B. L. Scott, R. Wu, R. Waterman, D. E. Morris, P. Yang, L. Gagliardi and J. L. Kiplinger, *Nature*, 2020, **578**, 563–567.
3 J. Gomes and R. Mallion, *Chem. Rev.*, 2001, **101**, 1349–1384.
4 E. Hückel, *Z. Phys.*, 1931, **70**, 204–286.
5 M. J. Cook, A. R. Katritzky and P. Linda, *Adv. Heterocycl. Chem.*, 1974, **17**, 255–356.
6 K. E. Horner and P. B. Karadakov, *J. Org. Chem.*, 2013, **78**, 8037–8043.
7 K. Najmidin, A. Kerim, P. Abdirishit, H. Kalam and T. Tawar, *J. Mol. Model.*, 2013, **19**, 3529–3535.
8 A. Wadsworth, M. Moser, A. Marks, M. S. Little, N. Gasparini, C. J. Brabec, D. Baran and I. McCulloch, *Chem. Soc. Rev.*, 2019, **48**, 1596–1625.
9 H. Usta, D. Kim, R. Ozdemir, Y. Zorlu, S. Kim, M. C. Ruiz Delgado, A. Harbuzaru, S. Kim, G. k. Demirel, J. Hong, Y. Ha, K. Cho, A. Facchetti and M. Kim, *Chem. Mater.*, 2019, **31**, 5254–5263.
10 Y. Lin, A. Magomedov, Y. Firdaus, D. Kaltsas, A. El-Labban, H. Faber, D. R. Naphade, E. Yengel, X. Zheng, E. Yarali, N. Chaturvedi, K. Loganathan, D. Gkeka, S. H. AlShammari, O. M. Bakr, F. Laquai, L. Tsetseris, V. Getautis and T. D. Anthopoulos, *ChemSusChem*, 2021, **14**, 3569–3978.
11 K. Feng, H. Guo, J. Wang, Y. Shi, Z. Wu, M. Su, X. Zhang, J. H. Son, H. Y. Woo and X. Guo, *J. Am. Chem. Soc.*, 2021, **143**, 1539–1552.
12 S. Shi, P. Chen, Y. Chen, K. Feng, B. Liu, J. Chen, Q. Liao, B. Tu, J. Luo, M. Su, H. Guo, M.-G. Kim, A. Facchetti and X. Guo, *Adv. Mater.*, 2019, **31**, 1905161.
13 X. Zhang, L. Qin, J. Yu, Y. Li, Y. Wei, X. Liu, X. Lu, F. Gao and H. Huang, *Angew. Chem., Int. Ed.*, 2021, **60**, 12475.
14 A. G. A. Sá, A. C. de Meneses, P. H. H. de Araújo and D. de Oliveira, *Trends Food Sci. Technol.*, 2017, **69**, 95–105.
15 P. Xing and Y. Zhao, *Adv. Mater.*, 2016, **28**, 7304–7339.
16 R. Breslow, J. Brown and J. J. Gajewski, *J. Am. Chem. Soc.*, 1967, **89**, 4383–4390.
17 J. L. Marshall, K. Uchida, C. K. Frederickson, C. Schutt, A. M. Zeidell, K. P. Goetz, T. W. Finn, K. Jarolimek, L. N. Zakharov, C. Risko, R. Herges, O. D. Jurchescu and M. M. Haley, *Chem. Sci.*, 2016, **7**, 5547–5558.
18 X. Fu, Y. Meng, X. Li, M. Stępień and P. J. Chmielewski, *Chem. Commun.*, 2018, **54**, 2510–2513.
19 A. Konishi, Y. Okada, M. Yasuda, A. Konishi, R. Kishi, M. Nakano and M. Yasuda, *J. Am. Chem. Soc.*, 2019, **141**, 560–571.
20 Y. Sun, Y. Guo and Y. Liu, *Mater. Sci. Eng., R*, 2019, **136**, 13–26.
21 Z. Wen and J. I. C. Wu, *Chem. Commun.*, 2020, **56**, 2008–2011.
22 X. Liu, Y. Wei, X. Zhang, L. Qin, Z. Wei and H. Huang, *Sci. China: Chem.*, 2021, **64**, 228–231.
23 H. U. Kim, J.-H. Kim, H. Suh, J. Kwak, D. Kim, A. C. Grimsdale, S. C. Yoon and D.-H. Hwang, *Chem. Commun.*, 2013, **49**, 10950–10952.
24 Z. Zhang, H. Fan and X. Zhu, *Org. Chem. Front.*, 2017, **4**, 711–716.

25 Z. Jin, Z. F. Yao, K. P. Barker, J. Pei and Y. Xia, *Angew. Chem., Int. Ed.*, 2019, **58**, 2034.
26 G. Dai, J. Chang, W. Zhang, S. Bai, K.-W. Huang, J. Xu and C. Chi, *Chem. Commun.*, 2015, **51**, 503–506.
27 G. Dai, J. Chang, X. Shi, W. Zhang, B. Zheng, K. W. Huang and C. Chi, *Chem. – Eur. J.*, 2015, **21**, 2019–2028.
28 F. Yin, L. Wang, X. Yang, M. Liu, H. Geng, Y. Liao, Q. Liao and H. Fu, *New J. Chem.*, 2020, **44**, 17552–17557.
29 H. Oshima, A. Fukazawa and S. Yamaguchi, *Angew. Chem., Int. Ed.*, 2017, **56**, 3270–3274.
30 A. Konishi, Y. Okada, M. Nakano, K. Sugisaki, K. Sato, T. Takui and M. Yasuda, *J. Am. Chem. Soc.*, 2017, **139**, 15284–15287.
31 C. K. Frederickson, B. D. Rose and M. M. Haley, *Acc. Chem. Res.*, 2017, **50**, 977–987.
32 J. Melidonie, J. Liu, Y. Fu, J. J. Weigand, R. Berger and X. Feng, *J. Org. Chem.*, 2018, **83**, 6633–6639.
33 F. G. Klärner, *Angew. Chem., Int. Ed.*, 2001, **40**, 3977–3981.
34 T. Nishinaga, T. Ohmae, K. Aita, M. Takase, M. Iyoda, T. Arai and Y. Kunugi, *Chem. Commun.*, 2013, **49**, 5354–5356.
35 T. Kawase, T. Fujiwara, C. Kitamura, A. Konishi, Y. Hirao, K. Matsumoto, H. Kurata, T. Kubo, S. Shinamura, H. Mori, E. Miyazaki and K. Takimiya, *Angew. Chem., Int. Ed.*, 2010, **49**, 7728–7732.
36 C. Liu, S. Xu, W. Zhu, X. Zhu, W. Hu, Z. Li and Z. Wang, *Chem. – Eur. J.*, 2015, **21**, 17016–17022.
37 M. Nakano, I. Osaka and K. Takimiya, *J. Mater. Chem. C*, 2015, **3**, 283–290.
38 A. D. Allen and T. T. Tidwell, *Chem. Rev.*, 2001, **101**, 1333–1348.
39 M. Baranac-Stojanovic, *Chem. – Eur. J.*, 2019, **25**, 9747–9757.
40 X.-Y. Wang, A. Narita, X. Feng and K. Müllen, *J. Am. Chem. Soc.*, 2015, **137**, 7668–7671.
41 J. Cao, G. London, O. Dumele, M. von Wantoch Rekowski, N. Trapp, L. Ruhlmann, C. Boudon, A. Stanger and F. Diederich, *J. Am. Chem. Soc.*, 2015, **137**, 7178–7188.
42 T. Yoshida, D. Sakamaki, S. Seki and H. Shinokubo, *Chem. Commun.*, 2017, **53**, 1112–1115.
43 Z. Jin, Y. C. Teo, S. J. Teat and Y. Xia, *J. Am. Chem. Soc.*, 2017, **139**, 15933–15939.
44 A. Konishi, Y. Okada, R. Kishi, M. Nakano and M. Yasuda, *J. Am. Chem. Soc.*, 2018, **141**, 560–571.
45 A. Facchetti, *Mater. Today*, 2013, **16**, 123–132.
46 J. Wu, D. Yang, Q. Wang, L. Yang, H. Sasabe, T. Sano, J. Kido, Z. Lu and Y. Huang, *J. Mater. Chem. A*, 2018, **6**, 5797–5806.
47 L. Yang, W. Gu, L. Lv, Y. Chen, Y. Yang, P. Ye, J. Wu, L. Hong, A. Peng and H. Huang, *Angew. Chem., Int. Ed.*, 2018, **57**, 1096.
48 F. S. Melkonyan, W. Zhao, M. Drees, N. D. Eastham, M. J. Leonardi, M. R. Butler, Z. Chen, X. Yu, R. P. Chang, M. A. Ratner, A. F. Facchetti and T. J. Marks, *J. Am. Chem. Soc.*, 2016, **138**, 6944–6947.
49 T. Hodsden, K. J. Thorley, J. Panidi, A. Basu, A. V. Marsh, H. Dai, A. J. P. White, C. Wang, W. Mitchell, F. Glöcklhofer, T. D. Anthopoulos and M. Heeney, *Adv. Funct. Mater.*, 2020, **30**, 2000325.
50 A. F. Paterson, S. Singh, K. J. Fallon, T. Hodsden, Y. Han, B. C. Schroeder, H. Bronstein, M. Heeney, I. McCulloch and T. D. Anthopoulos, *Adv. Mater.*, 2018, **30**, 1801079.
51 L. Duan, J. Qiao, Y. Sun and Y. Qiu, *Adv. Mater.*, 2011, **23**, 1137–1144.
52 J. Fan, M. Hu, P. Zhan and X. Peng, *Chem. Soc. Rev.*, 2013, **42**, 29–43.
53 M. He, C. Li, Z. Pang, K. Chen, Y. Tan, Y. Huang and Z. Lu, *Chem. – Eur. J.*, 2020, **26**, 12140–12144.
54 M. Nakano, I. Osaka, K. Takimiya and T. Koganezawa, *J. Mater. Chem. C*, 2014, **2**, 64–70.
55 D. C. Grenz, M. Schmidt, D. Kratzert and B. Esser, *J. Org. Chem.*, 2018, **83**, 656–663.
56 R. Ozdemir, S. Park, İ. Deneme, Y. Park, Y. Zorlu, H. A. Alidagi, K. Harmandar, C. Kim and H. Usta, *Org. Chem. Front.*, 2018, **5**, 2912–2924.
57 Y. Zeng, R. Duan, Y. Guo, G. Han, Q. Li and Y. Yi, *Chin. Chem. Lett.*, 2019, **30**, 211–216.
58 D. J. Schipper, L. C. Moh, P. Müller and T. M. Swager, *Angew. Chem., Int. Ed.*, 2014, **53**, 5847–5851.
59 T. Bally, S. Chai, M. Neuenschwander and Z. Zhu, *J. Am. Chem. Soc.*, 1997, **119**, 1869–1875.
60 N. Baird and R. West, *J. Am. Chem. Soc.*, 1971, **93**, 3072–3073.
61 J. Zhao, K. Oniwa, N. Asao, Y. Yamamoto and T. Jin, *J. Am. Chem. Soc.*, 2013, **135**, 10222–10225.
62 A. Konishi, Y. Okada, M. Nakano, K. Sugisaki, K. Sato, T. Takui and M. Yasuda, *J. Am. Chem. Soc.*, 2017, **139**, 15284–15287.
63 C. Hu and Q. Zhang, *Chin. J. Chem.*, 2013, **31**, 1404–1408.
64 S.-i. Kato, S. Kuwako, N. Takahashi, T. Kijima and Y. Nakamura, *J. Org. Chem.*, 2016, **81**, 7700–7710.
65 H. Xi, Z. Zhang, W. Zhang, M. Li, C. Lian, Q. Luo, H. Tian and W.-H. Zhu, *J. Am. Chem. Soc.*, 2019, **141**, 18467–18474.
66 G. London, M. von Wantoch Rekowski, O. Dumele, W. B. Schweizer, J.-P. Gisselbrecht, C. Boudon and F. Diederich, *Chem. Sci.*, 2014, **5**, 965–972.
67 S. Bradamante, A. Facchetti and G. A. Pagani, *J. Phys. Org. Chem.*, 1997, **10**, 514–524.
68 T. J. Aldrich, M. Matta, W. Zhu, S. M. Swick, C. L. Stern, G. C. Schatz, A. Facchetti, F. S. Melkonyan and T. J. Marks, *J. Am. Chem. Soc.*, 2019, **141**, 3274–3287.
69 J. H. Park, E. H. Jung, J. W. Jung and W. H. Jo, *Adv. Mater.*, 2013, **25**, 2583–2588.
70 W. Zhu, J. M. Alzola, T. J. Aldrich, K. L. Kohlstedt, D. Zheng, P. E. Hartnett, N. D. Eastham, W. Huang, G. Wang, R. M. Young, G. C. Schatz, M. R. Wasielewski, A. Facchetti, F. S. Melkonyan and T. J. Marks, *ACS Energy Lett.*, 2019, **4**, 2695–2702.
71 J. Chen, X. Zhuang, W. Huang, M. Su, L.-w. Feng, S. M. Swick, G. Wang, Y. Chen, J. Yu, X. Guo, T. J. Marks and A. Facchetti, *Chem. Mater.*, 2020, **32**, 5317–5326.